

# Fabrication and First Characterization of Silicon-Based Full 3-D Microdosimeters

Angela Kok<sup>1</sup>, Marco Povoli<sup>1</sup>, Anand Summanwar, Linh T. Tran<sup>2</sup>, *Member, IEEE*,  
 Marco Petasecca<sup>1</sup>, *Member, IEEE*, Michael L. F. Lerch<sup>2</sup>, *Member, IEEE*, David Bolst<sup>2</sup>, *Member, IEEE*,  
 Susanna Guatelli, *Member, IEEE*, and Anatoly B. Rosenfeld<sup>2</sup>, *Senior Member, IEEE*

**Abstract**—Microdosimetry provides measurements of stochastic lineal energy deposition in a micrometric sensitive volume (SV) that are comparable to human cell dimensions, typically in the order of 10–15  $\mu\text{m}$  in diameter. Silicon-based microdosimeters have been fabricated using “3-D technology,” providing true cell-like SVs that are fully encapsulated by a 3-D through substrate electrode. The unique geometry has been made feasible using modern microelectromechanical systems (MEMS). The combination of MEMS techniques and radiation detector fabrication brings forth challenges in achieving reliability, consistency, and high yield. This article reviews the technological challenges encountered in several prototype runs completed at SINTEF. The technological review and prototype iterations aim to deliver a future technology plan at the manufacture level with a high yield throughput.

**Index Terms**—3-D detector, heavy ion therapy (HIT), microdosimetry, microsystem, radiation detector, silicon detector, silicon fabrication technology.

## I. INTRODUCTION

MICRODOSIMETRY is the measurement of stochastic energy depositions in sensitive volumes (SVs) [1] of micrometric scale. The SVs are comparable to the size of biological cells. This unique concept of microdosimetry provides the dose equivalent from a mixed radiation field and important information such as radiobiological effectiveness (RBE), a major advantage over conventional dosimetry where only the absorbed dose for a known radiation field is measured. Currently, Tissue Equivalent Proportional Counter (TEPC) is the gold standard in microdosimetry [2]. They, however, have disadvantages such as wall effect, high-voltage operation, and large physical size that are not ideal for microdosimetry. Their spatial resolution is also insufficient for the required

micrometric precision around the Bragg peak that contains vital information for a novel heavy-ion therapy (HIT). In recent years, attempts to miniaturize TEPCs have been carried out [3]. However, the inconvenient use of gas detection and their low spatial resolution remain nonideal for the intended applications such as quality assurance and treatment planning for HIT. Silicon technology is well established, matured, and has for several decades provided the nuclear science and medical community with reliable sensors that are small and compact, with easy coupling to readout electronics that offers real-time online monitoring. Silicon-based microdosimeter is thus an attractive candidate, especially for the growing demands of improved dosimetry methods with precise RBE prediction in radiation protection and particle therapy.

Silicon-based microdosimeter was first proposed by the Centre for Medical Radiation Physics (CMRP) at University of Wollongong, Australia, to address the shortcomings of TEPCs. Such microdosimeter is based on an array of micrometer-sized SVs fabricated on silicon-on-insulator (SOI) substrates that mimic an array of biological cells. The SOI approach allows the formation of SVs with dimensions closer to the size of biological cells with respect to a full silicon substrate approach. Using SOI technology, an active layer, much thinner than a standard silicon substrate, can be achieved, usually around 10- $\mu\text{m}$  thick. The active layer is typically supported by a thicker substrate of around 300  $\mu\text{m}$  but isolated by a thin layer of silicon dioxide. The first silicon-based microdosimeter was fabricated and studied by CMRP in 2001. Since then, several generations of silicon-based microdosimeters have been proposed and fabricated, with each generation optimizing the previous one [4]–[10].

Silicon sensors including those fabricated on SOI substrates are typically manufactured using silicon planar technology, where the electrodes are formed on the surface of the substrates. Using planar technology, the SVs are fully encapsulated, and a true mimic of biological cells is not achieved. Cross-talks between SVs have been observed. In 2013, a collaboration between SINTEF and CMRP began to investigate the feasibility of using one of the latest developments in silicon radiation detectors in microdosimetry, the “3-D technology” [11]. 3-D technology was first proposed by Parker *et al.* [12] for high-energy physics, and the concept was later developed by several other European cleanroom facilities [13]–[16]. In 3-D technology, the electrodes penetrate through the entire

Manuscript received August 11, 2020; revised October 9, 2020; accepted October 27, 2020. Date of publication October 30, 2020; date of current version December 16, 2020. This work was supported in part by the Research Council of Norway via the NANO2021 Program under Project 21994 and in part by the Australian Research Council under Grant DP170102273.

Angela Kok, Marco Povoli, and Anand Summanwar are with SINTEF MiNaLab, Oslo 0373, Norway (e-mail: angela.kok@sintef.no; marco.povoli@sintef.no; anand.summanwar@sintef.no).

Linh T. Tran, Marco Petasecca, Michael L. F. Lerch, David Bolst, Susanna Guatelli, and Anatoly B. Rosenfeld are with the Centre for Medical Radiation Physics (CMRP), University of Wollongong, Wollongong, NSW 2522, Australia (e-mail: ltt822@uowmail.edu.au; marcop@uow.edu.au; mlerch@uow.edu.au; dbolst@uow.edu.au; susanna@uow.edu; anatoly@uow.edu.no).

Color versions of one or more figures in this article are available at <https://doi.org/10.1109/TNS.2020.3035077>.

Digital Object Identifier 10.1109/TNS.2020.3035077

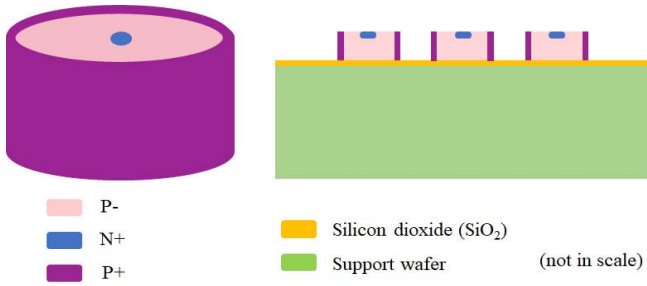


Fig. 1. (Left) A single SV. (Right) The cross section of a completed wafer where the SVs situated are insulated by a thin layer of  $\text{SiO}_2$  from the support.

substrate [11] and an SV can, therefore, be fully encapsulated by a ring-like through substrate electrode. The collaboration anticipated that 3-D microdosimeters will provide a close-to-ideal mimic of biological cells, while offering all the advantages from silicon detectors.

The unique geometry of 3-D sensors provides many advantages compared to conventional silicon sensors: low operating voltage, radiation hardness, and fast time response. The technology has been made possible by a combination of long-standing expertise in silicon radiation sensors and modern development in microelectromechanical systems (MEMS), the key breakthrough being deep reactive ion etching (DRIE) [17] and wafer bonding. Institute of Microelectronics of Barcelona-Centre Nacional de Microelectronica (IMB-CNM) investigated a similar technology that implemented small arrays ( $10 \times 10$ ) of SVs where the SVs are not fully encapsulated [18]. Our concept centers in fully encapsulated SVs that are embedded in a tissue equivalent material. Similar embedment concept has also been previously explored for other dosimetry applications [19].

The proposed SVs have a diameter of between 10 and 15  $\mu\text{m}$ , like a biological cell, encapsulated by a circular 3-D electrode, as shown in Fig. 1 (left). These small dimensions together with using MEMS technologies in radiation detector bring forth many challenges. Several prototype runs have been completed at SINTEF Minalab, with an aim to address the foreseen challenges and to deliver a reliable technology plan for future manufacture. Many working devices have been fabricated and fully characterized at HIT facilities. The first results are in excellent agreement with those obtained from TEPCs [20]. In this article, we present, review, and discuss the overall technology investigation and the challenges throughout the prototype runs, forming a basis for a future technology plan at manufacture level.

## II. SILICON MICRODOSIMETER TECHNOLOGY

### A. Technology Overview

DRIE is the key in 3-D technology, but when implemented in a radiation detector, the technique poses many challenges. Following DRIE, planarization of wafer surfaces is vital to facilitate subsequent fabrication steps. The etched structures where silicon is removed are usually planarized by filling them with either polycrystalline silicon (poly-Si) or low-temperature deposition of silicon dioxide. Despite planarization, topography usually remains over the filled structures.

TABLE I  
FABRICATION STEPS

Step	Description	Mask Layer/Electrode
#1	p-spray implantation	
#2	First oxidation	
#3	Photolithography	p-electrode
#4	Deep Reactive Ion Etching	p-electrode
#5	Doping	p-electrode
#6	Filling of electrodes (in some cases)	p-electrode
#7	Oxidation	p-electrode
#8	Photolithography	n-electrode
#9	Implantation	n-electrode
#10	Oxidation	n-electrode
#11	Photolithography	Contact
#12	Metal deposition	
#13	Photolithography	Metal
#14	Photolithography	Mushroom
#15	Silicon etching	Mushroom
#16	Polyimide deposition	

A summary of key fabrication steps for 3D silicon microdosimeters

This adds complication in the photolithographic process causing diffusion, reflection, and refraction of UV light during the patterning process. The topography also affects the metal bus lines that must bypass these structures.

Photolithography is normally a well-established process. However, using current standard mask aligners, implementing several photolithography layers within a single SV that has a diameter of about 15  $\mu\text{m}$  is reaching the spatial limit of the equipment. This together with the topography formed by the DRIE process, maintaining high precision in photolithography is a major challenge. More advanced equipment such as a wafer stepper with a higher spatial resolution could be a better choice.

The overall technology plan for 3-D microdosimeters is summarized in Table I. The fabrication begins with a p-spray implantation and high-temperature oxidation. The process is then followed by the formation of P+ and N+ electrodes. Finally, the devices are completed by depositing and patterning the metal bus lines for reading out and biasing the electrodes. The P+ electrodes are formed by first etching the 3-D microstructures using DRIE, the so-called Bosch process [17]. The process consists of cyclic isotropic etching and fluorocarbon-based protection film deposition by quick gas switching. The key to a successful etching result is the perfect tuning of alternating cycles of etching and protection. Once the 3-D microstructures are formed, they are then doped by gas-phase doping for the P+ electrodes. Following gas-phase doping, the structures are then filled with polycrystalline silicon (poly-Si). The N+ electrode is created by surface ion implantation. Several photolithography steps are then performed to complete the devices. This includes metal connections and opening in the oxide that allows the metal lines to connect to the corresponding electrodes. On some wafers, the excess silicon outside of the SVs was removed once the SVs are completed. The gap was then filled with a tissue equivalent material such as polyimide. The overall baseline technology plan in all prototype runs follow the one as described in Table I but various detailed fabrication and design parameters were also implemented.

## B. Design Overview

The design of a 3-D microdosimeter begins from the configuration of a single SV. Each SV is essentially a single p-n junction diode, typically has a diameter of between 10 and 15  $\mu\text{m}$ . In our prototype runs, the SVs are fabricated on a 10- $\mu\text{m}$  thick p-type high-resistivity silicon substrate that is known as the “device layer.” The device layer is attached to a 300- $\mu\text{m}$ -thick supporting substrate, isolated by a thin layer of silicon dioxide. Other thicknesses such as 5 and 20  $\mu\text{m}$  were also implemented for specific applications. This article will focus on the results from 10- $\mu\text{m}$ -thick devices. The signal induced in a single SV is measured by the junction electrode (N+) situated in the center of the SV. Fig. 1 shows how the SVs are implemented in the device layer of an SOI substrate. In the first prototype run, two diameters, 18 and 30  $\mu\text{m}$ , were chosen. Both are designed to be larger than a typical biological cell to reduce the difficulties in fine photolithography resolution. However, the effective diameters for both designs are expected to be approximately 13 and 25  $\mu\text{m}$  following DRIE and high-temperature processes. DRIE widens the structures, while high temperature drives the dopants further from the surface. The wider diameter of 30  $\mu\text{m}$  that do not reach the limit of our fine line lithography was implemented as a benchmark. In an SV with a diameter of 18  $\mu\text{m}$ , the overlap between the necessary photolithographic layers and the interelectrode distance (between the N+ and P+ electrodes) are extremely small. When reaching this limit, one can observe low breakdown and high leakage current. In the worst case scenario, the margins in alignment and linewidths could be so large that the P+ and N+ electrodes can be shorted after dopant diffusion. All precautions were considered in the design phase to avoid this scenario. In the worst case, where no SVs with 18- $\mu\text{m}$  diameter are functional, devices with larger diameters will provide a mean for identifying the cause of nonfunctional devices. Following the electrical, functional, and simulation results from the first prototype run, an optimized diameter of 22  $\mu\text{m}$  was chosen in the second and the third prototype runs.

Once the geometry of the SVs was defined, SVs were arranged in arrays. The number of SVs in each array was chosen upon an intended application. Several different sensor layouts were implemented. The main parameters that determine the total number of SVs are the expected dose rate and radiation flux. The details will not be discussed in this article. In this article, results from devices that have  $20 \times 20$  (400) and  $50 \times 50$  (2500) SVs will be discussed. Fig. 2 shows how the ohmic (P+) and junction (N+) electrodes were drawn at the design stage according to each necessary photolithographic layer, as implemented on the top surface of the device layer. The design consists of five photolithographic layers. DRIE is the mask layer used for the (DRIE) process that will later become the P+ electrodes. P+ and N+ are the mask layers for doping and creating the P+ and N+ electrodes, respectively. Photolithographic layer (CONT) opens the contact holes once the electrodes are completed. A layer of aluminum is then deposited and patterned using the METAL layer. Two SV designs, the full 3-D microdosimeter (F3D) and the two half-

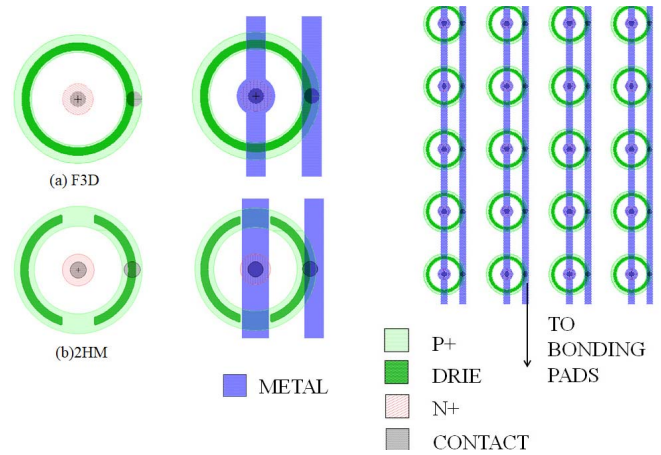


Fig. 2. Design of 3-D microdosimeters. Left: the cell is surrounded by a 3-D P+ electrode and the measured signal is read out by the central N+ electrode. (a) Full 3-D (F3D) and (b) 2HMs. Middle/right: electrodes are connected by metal lines, arranged to suit specific applications.

moon designs (2HM) were implemented for further technology investigations.

The design shown on the top of Fig. 2(a) is the “full 3-D microdosimeter (F3D),” the first initial design where the P+ electrode fully encapsulates the entire SV. The biggest challenge in this design is to achieve reliable connections to the central N+ electrodes, as the metal bus lines must bypass through the substrate P+ electrodes. Although the surface over the P+ electrodes is planarized by filling the etched structures with poly-Si, there is still a high topography and sometimes a small gap. An alternative design, the 2HM configuration was, therefore, proposed and implemented, as shown in the bottom of Fig. 2(b). In this configuration, the P+ electrode is split into two essentially 2HM shapes. The space between the 2HM provides a perfectly flat surface so that the metal bus line connecting the N+ electrodes does not need to bypass any topography or physical gap of the P+ electrode, as in the F3D design. The 2HM design ensures that all N+ electrodes are connected, eliminating the uncertainty of poor metal connection in the F3D design. Besides the five layers shown in Fig. 2, an additional layer, “MUSHROOM” was also designed to remove all excess silicon outside of the SVs. Following the removal of excess silicon outside of the SVs, the gap is then filled with a tissue equivalent polymer. In the first prototype run, the “MUSHROOM” layer was implemented on the F3D devices. For clarification, devices that have this extra layer will be referred to as the “full 3-D mushroom microdosimeter (F3DM).” The three design configurations are summarized in Table II. Since all F3DM devices are also F3D devices, all electrical measurements and simulation in this article will primarily focus on the F3D devices.

## III. SIMULATION

Throughout the prototype development, the design was investigated and validated by numerical simulations, using SYNOPSIS TCAD tools [21]. The simulator gave the expected electrical and functional characteristics and assisted

TABLE II  
DESIGN CONFIGURATIONS

Type	Name	Description
<i>2HM</i>	Half-moon	Circular P+ ring electrode split into two half-moons
<i>F3D</i>	Full 3D	A complete circular P+ ring electrode
<i>F3DM</i>	Full 3D Mushroom	As full 3D with excess silicon outside of SV removed and replaced by a tissue equivalent polymer

Three design configurations implemented in 3D microdosimeter.

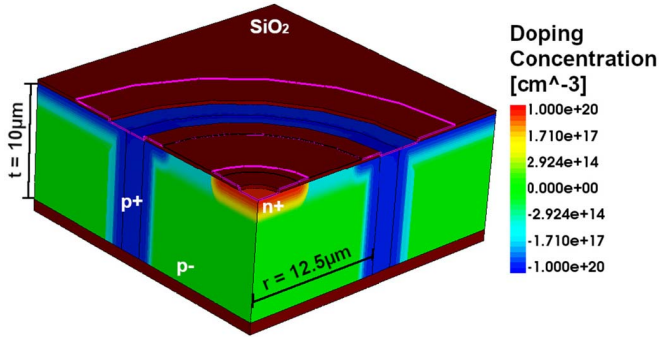


Fig. 3. Simulated structure for a full 3-D microdosimeter (F3D). Given the symmetry of the real structures, only a quarter is simulated.

in deciding on the optimal process and design parameters such as the sensor thickness and the diameter of the SV. Fig. 3 shows the simulated structure of a full 3-D microdosimeter (F3D) fabricated on a 10- $\mu\text{m}$ -thick device layer. Three-dimensional simulation of this structure requires an extremely long computation time. For this reason, only a quarter of an SV was simulated, and the results were scaled to the full sensor size exploiting the cylindrical symmetry of the SV structure. Two-dimensional simulation with a shorter computation time was also performed but the results using 3-D was found to be more accurate. The 3-D simulation result is, therefore, presented here in this article. The simulated structure is based on the dimensions used in the second and third prototypes where the dimensions, depth, and doping concentration of the electrodes were optimized using the results of the first prototype run.

In this simulated structure, the thickness of the active layer is 10  $\mu\text{m}$  and the cylindrical ring that encapsulates the SV has a radius of 12.5  $\mu\text{m}$ , a diameter of 25  $\mu\text{m}$ , the same as the diameter implemented in the second and the third prototype runs. Using this model, electrical properties such as  $I - V$  and  $C - V$  characteristics were simulated. This was carried out with the N+ electrode set to ground while ramping down the voltage on the P+ electrode from 0 to  $-100$  V. The simulated current and capacitance were extracted from the N+ electrode, as plotted in Fig. 4. The simulated quantities were scaled to a full microdosimeter device that corresponds to a sensor consists of an array of  $20 \times 20$  (400) SVs. The simulated  $C - V$  curve (red squares) decreases rapidly and starts saturating before a bias of 10 V bias, suggesting that the

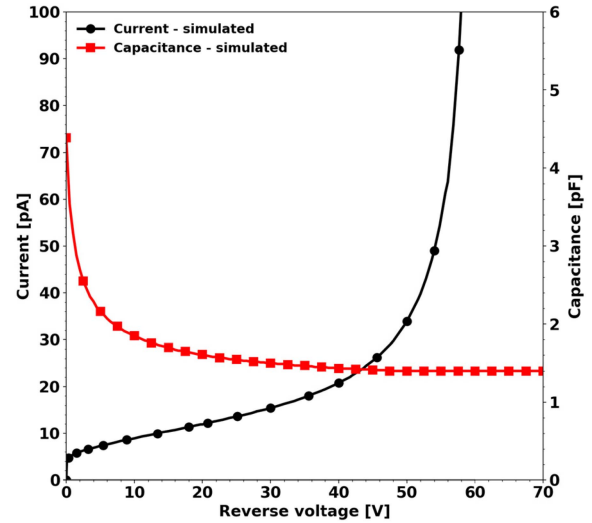


Fig. 4. Numerical simulation results for reverse current (black dots) and reverse capacitance (red squares).

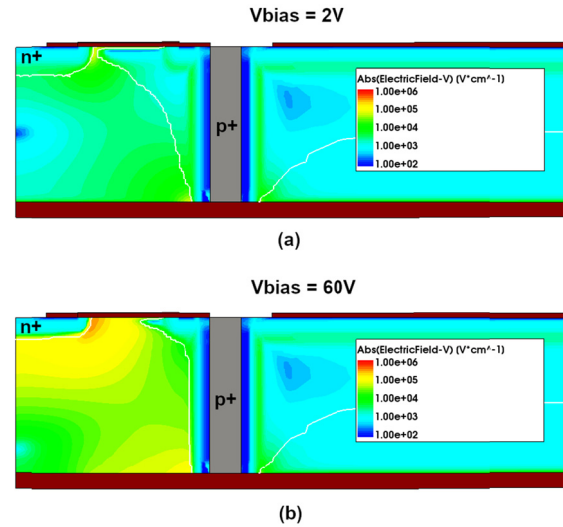


Fig. 5. Electric field distribution inside the SV at a bias voltage (a) 2 V and (b) close to breakdown at  $-60$  V.

full depletion of the SV is reached very quickly. The simulated current (black) was about 10 pA for the full scaled device at a bias voltage of 20 V, while the simulated breakdown voltage was around 55–60 V.

The 3-D electric field distribution for the quartered cell was simulated for all biasing conditions. The field distribution inside the SV at 2 and 60 V was extracted from a 2-D cross section along the radius of the SV, as shown in Fig. 5. The peak of the electric field was found, as expected, at the curvature of the p-n junction. At the bottom of the SV, the electric field was observed to be higher close to the lower part of the through substrate P+ electrode. The electric field directly below the N+ electrode is lower than desired, a region that will result in lower charge collection efficiency. This could be solved either by implanting the backside of the device layer prior to wafer bonding or by using silicon-on-silicon substrates

where the support wafer is highly doped and can be used as a backside P+ electrode. There are, however, some unknowns in this technological approach, which will be investigated in future prototype runs.

The second part of the numerical simulation was to illustrate the functional properties of 3-D microdosimeter by injecting simulated free charge carriers, minimum ionizing particles (MIPs) passing through the SVs, using the heavy-ion model from SYPNOSIS. In this study, a MIP was simulated to hit the SV at different positions along its radius in steps of  $1 \mu\text{m}$  (starting from the center of the N+ electrode). Each event was simulated for multiple biasing conditions. The simulated current pulses induced by the MIP were numerically integrated over a time period of  $1 \mu\text{s}$  to obtain the total collected charge by the sensor for each event.  $1 \mu\text{s}$  was used as this is the shaping time normally used in experiments. The simulated integrals are plotted as a function of hit positions in Fig. 6 for bias voltages of 1 and 10 V. It was observed that the bias voltage has almost no influence on the total charge collection efficiency for an integration time of  $1 \mu\text{s}$ . This confirms that, when using sufficiently long integration time, the sensors can essentially function in passive mode with zero bias. From the charge collection efficiency distribution over the entire radius of the SV, a reduced efficiency was observed in the area where the hit position was between 0 and  $4 \mu\text{m}$ , right below the N+ electrode. The reduced efficiency in this area is due to the higher recombination of generated charge in the highly doped N+ region. Beyond this point, the charge collection was found to be uniform until the hit position starts exiting the 3-D P+ electrode delimiting the SV (at around  $12 \mu\text{m}$ ). No charge was collected outside the P+ electrode, as expected. The simulation results confirmed the well-defined SV offered by this unique design of SV using the 3-D technology, where no signal is collected outside the SV and thus excellent isolation between the SVs can be achieved. The numerical simulations demonstrated the expected electrical and functional characteristics of the proposed design and technology.

#### IV. RESULTS

##### A. Fabrication

The design of the sensor and SVs was fully implemented on a 150-mm wafer layout. The fabrication steps were then carried out as summarized in Table I. A completed wafer from the first prototype run is shown in Fig. 7, illustrating the complete wafer layout with sensors of various sizes and designs. Standard planar processes such as thermal oxidation and ion implantation were performed with ease as expected. The implemented aspect ratio (depth-to-width ratio) of the P+ electrodes was between 3:1 and 5:1, well within the capability of DRIE process. However, maintaining a high precision and conformity throughout the etched structure required optimization. The correct cycling between plasma protection deposition and etching was tested to deliver a DRIE process for the P+ electrodes. Fig. 8 shows an etched circular ring structure after DRIE. The structure would later be doped and become the P+ electrode. Conformity was achieved, and no wall damage was observed. The cyclic etching in the Bosch process is evident

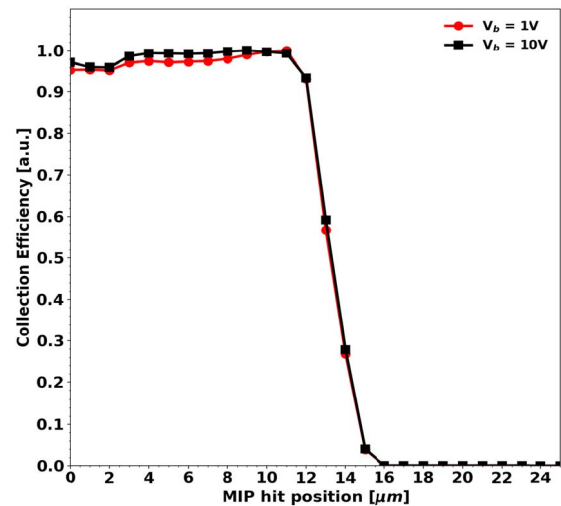


Fig. 6. Simulated charge collection efficiency in response to a MIP scanned across the radius of the SV. Two different operating voltages are shown, 1 and 10 V.

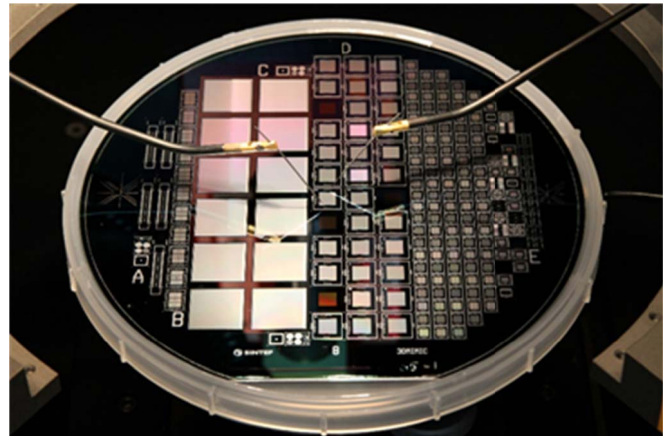


Fig. 7. Completed wafer of 3-D microdosimeters.

in the scalloped vertical wall of the etched structure. The same DRIE process was also used to etch the 2HM design as described in Fig. 2.

The etched circular ring was doped by gas-phase doping using boron tribromide ( $\text{BBr}_3$ ) and filled with polycrystalline silicon (poly-Si) by low-pressure chemical vapor deposition (LPCVD) at  $700^\circ\text{C}$ . Deposition of poly-Si is, however, not selective. The LPCVD process deposits poly-Si inside the 3-D structure as well as on the entire wafer surface.

The excess poly-Si on the wafer surface was removed before proceeding on further fabrication steps. The removal process can be made selective by using a photoresist mask that covers the P+ electrodes. However, this created a high topography over the P+ electrode. Optimized nonselective removal of poly-Si was used to remove the poly-Si in the second and third runs. Despite many optimizations of this process, a gap inside the P+ electrode was often observed after the removal, as shown in the SEM micrograph in Fig. 9. Although this gap is small, usually in the order of a few hundred nm, it can cause major disruptions in the metal line connection to the central

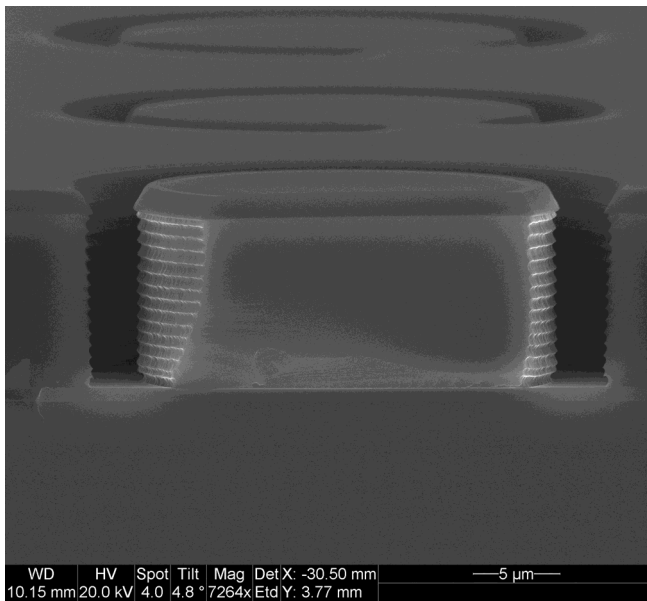


Fig. 8. Scanning electron microscope image of a circular 3-D ring formed and etched by DRIE.

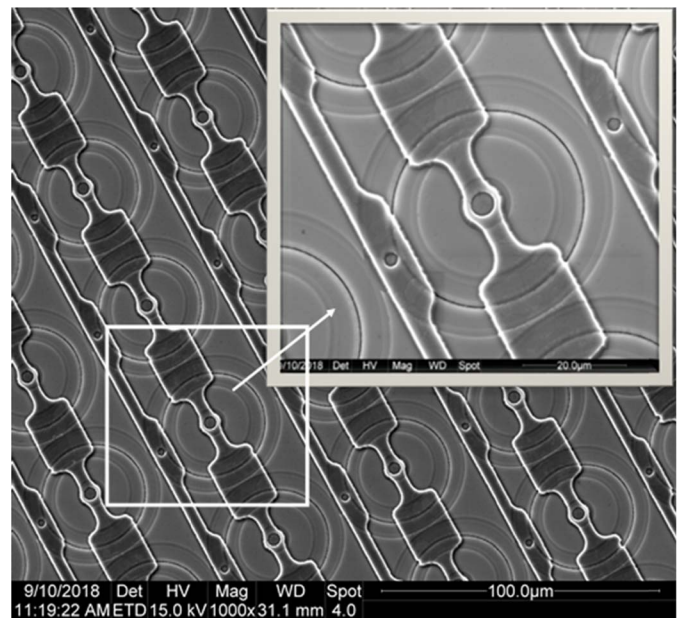


Fig. 10. Scanning electron microscope images taken for arrays of 3-D microdosimeters. The metal lines are intact in this case.

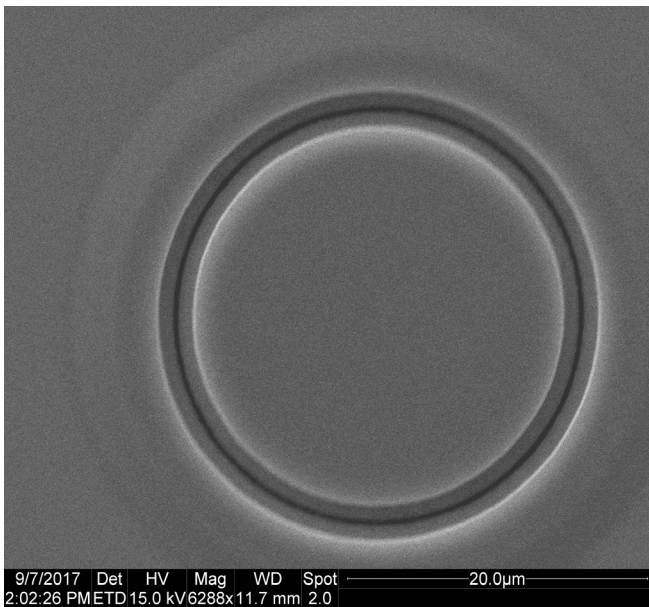


Fig. 9. Scanning electron microscope image of a circular 3-D ring. A small gap was observed despite process optimization.

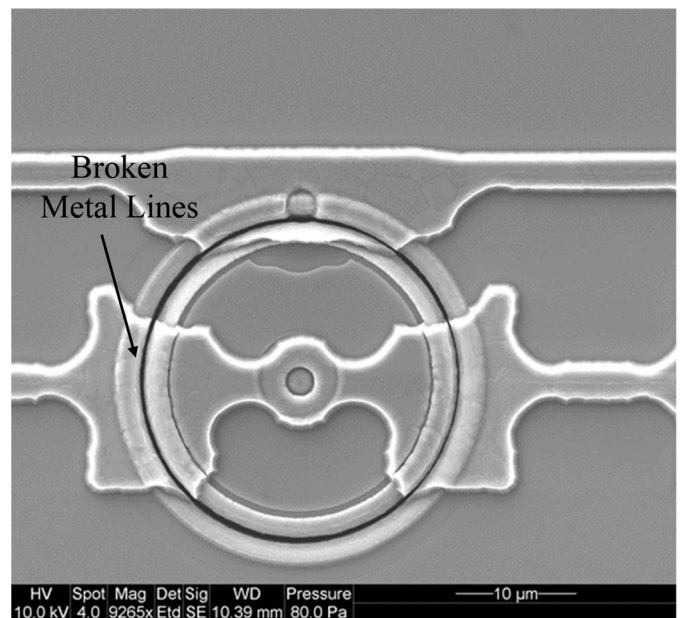


Fig. 11. Scanning electron microscope image of a completed SV where the metal line connecting the central N+ electrode is clearly broken.

N+ electrode. The width of this gap also varies from sensor to sensor and across the wafer. In most devices, the metal lines were intact. One example is shown in Fig. 10 where arrays of SVs were clearly connected successfully. Broken metal lines were, however, observed in some devices (Fig. 11). Since this issue varies greatly across a wafer and within one batch, it is a yield factor that is extremely difficult to monitor. This issue was already foreseen and was the reason that the 2HM design was implemented. As mentioned previously, the 2HM design, however, does not deliver the promise of an encapsulated SV, and the F3D and F3DM remain to be the ultimate design of

choice, even though the (2HM) do not have this connection issue. This will be further optimized in future prototype runs.

From the completed wafers, two were then selected for the full 3-D mushroom (F3DM) implementation, in which excess silicon outside the SVs was removed and the gaps were filled with a tissue equivalent material. Prior to the removal, the SVs and metal lines were protected by a layer of patterned photoresist. The key challenge in this process is to remove the excess silicon without damaging the completed structures.

The optimized plasma etching process was first carried out on some test wafers. Fig. 12 shows how the SVs and



Fig. 12. Scanning electron microscope image showing a part of a sensor after excess silicon outside the SV was removed using plasma etching.

metal lines are maintained after the silicon was removed. One wafer was then coated with a tissue equivalent polymer, and, in this case, polyimide was used. Other common alternatives such as polymethylmethacrylate (PMMA) would also be a good candidate. Filling and planarizing these large voids are challenging when using a viscous polymer. The gaps between the SVs are wide and they stand at  $10\ \mu\text{m}$  above the supporting material. The viscosity and annealing process must be chosen correctly to achieve optimal filling. Several depositions with various annealing temperatures and conditions were performed in this first investigation. Fig. 13 shows the surface topography after the deposition of polyimide. The surface was not fully planarized despite process optimization, but most area outside the SVs was filled, and minimal presence of air bubbles trapped in the polymer was observed. The polyimide was subsequently patterned to allow access for the metal pads. This deposition process will be further optimized using other coating method such as spray coating in future runs.

### B. Electrical Measurements

Electrical measurements were carried out on selected devices of the different design configurations: half-moon (2HM), full 3-D (F3D), and full 3-D mushroom (F3DM). The measured devices from the first prototype run have a substrate thickness of  $10\ \mu\text{m}$ . Each device had a total of 2500 SVs fabricated in the first and the second runs. For all measured devices, all 2500 SVs were connected in the design. In the first prototype run, each SV has a diameter of either 18 or  $30\ \mu\text{m}$ , while in the second prototype run, the diameter was  $25\ \mu\text{m}$ .

Fig. 14 shows the capacitance–voltage ( $C-V$ ) measurement obtained from a full 3-D microdosimeter (F3D) fabricated in the first prototype run. The curve shows the capacitance decreases rapidly with increasing bias voltage from 0 to 2 V. Above 1 V, the capacitance begins to saturate, indicating

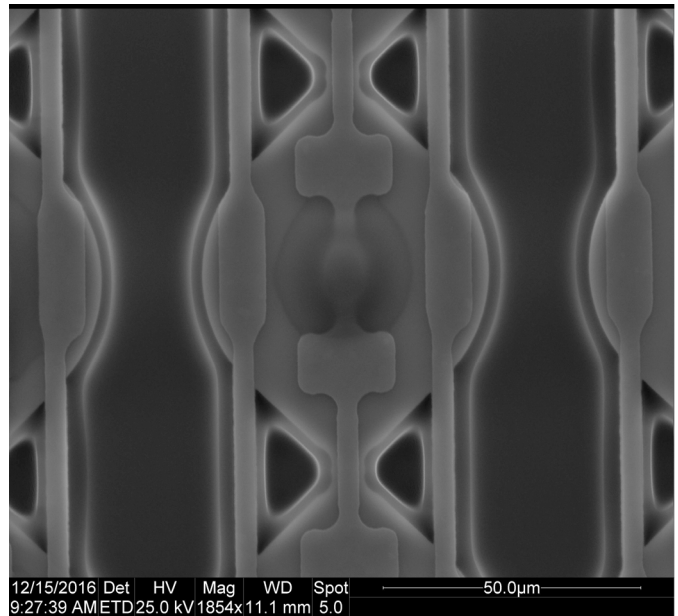


Fig. 13. Layer of polyimide was deposited by several iterations of spin coating.

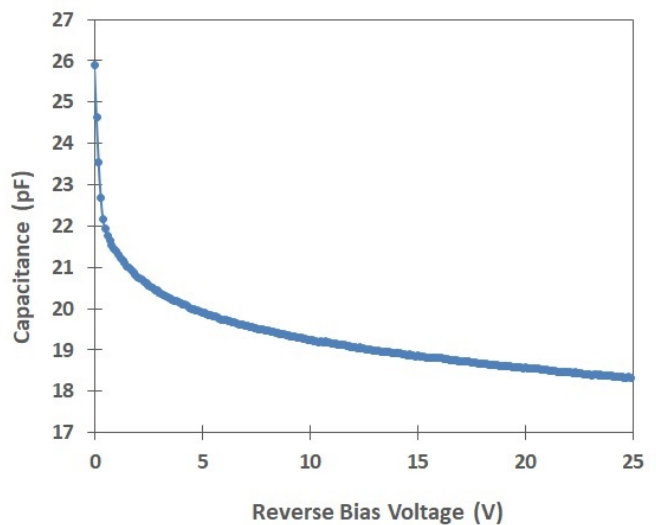


Fig. 14.  $C-V$  measurements performed on an F3D device from the first prototype run.

that the bulk is fully depleted. However, the capacitance never reaches full saturation. This is a well-understood effect for n-on-p detectors where a p-spray surface isolation is used. The continuous decrease in capacitance is caused by the gradual lateral depletion of the p-spray surface implant. The capacitance value at full depletion (e.g., for bias voltage greater than 2 V) is high, a major disadvantage of 3-D technology, where the interelectrode distance is short. In addition, the design of 3-D microdosimeters that feature long metal lines also add significant stray capacitance contribution due to the MOS effects under the metal connections. Considering the SVs alone, the full depletion voltage is shown to be very low, about 2 V, very close to the self-depletion point.

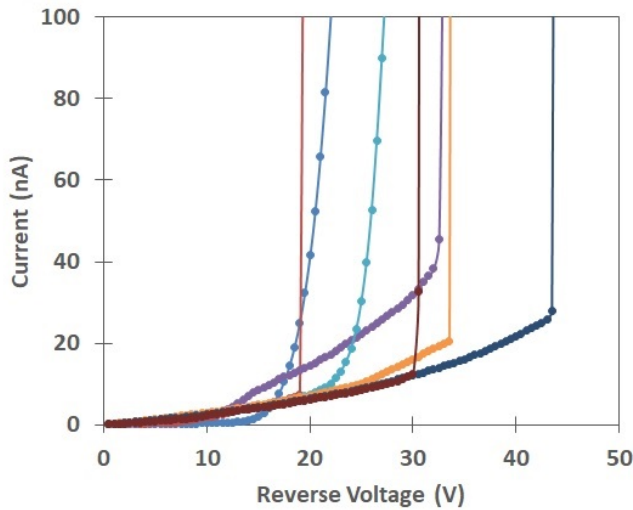


Fig. 15.  $I - V$  measurements on selected devices with 2HM design.

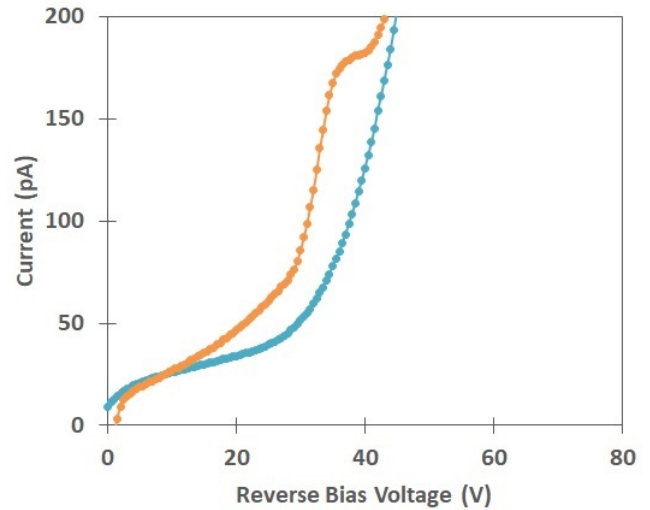


Fig. 17.  $I - V$  measurements taken from devices with full 3-D mushroom (F3DM) configuration from the first prototype run.

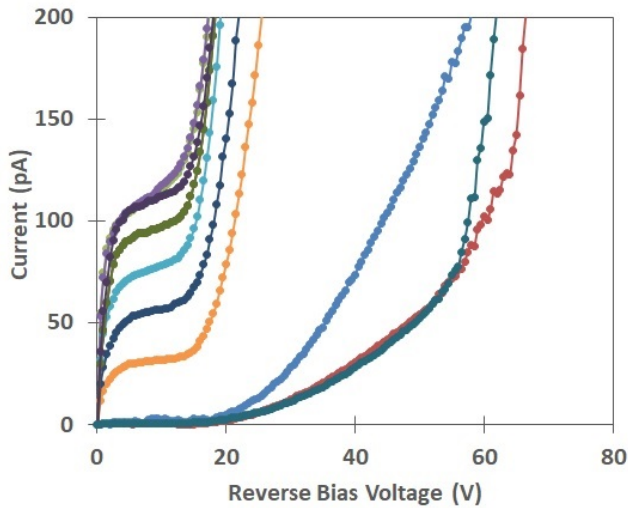


Fig. 16.  $I - V$  measurements taken from devices with full 3-D (F3D) configuration from the first prototype run.

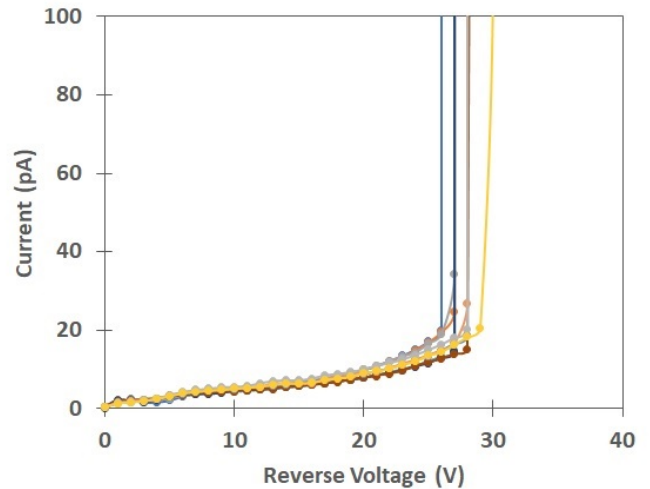


Fig. 18.  $I - V$  measurements taken from devices with full 3-D (F3D) configuration from the second prototype run.

$I - V$  measurements of the three designs (2HM, F3D, F3DM) from the first prototype run are shown in Figs. 15–18. Fig. 15 corresponds to the measured  $I - V$  on the 2HM devices, and Figs.16 and 18 are  $I - V$  measured on the F3D devices from the first and second prototype runs, respectively. All  $I - V$  measurements together with the  $C - V$  measurement demonstrated that fully functional 3-D microdosimeters have been successfully fabricated.

In Fig. 15, the  $I - V$  measurement for the 2HM design continues to increase at a higher degree when compared to the simulation when the bias voltage increases. In the 2HM configuration, the SVs are not fully enclosed. As the voltage further increases beyond the depletion of the SVs, the depletion from the central N+ electrode continues through the gap between the 2HMs, resulting in further current injection. Since only a quarter of an SV was simulated, this was not considered in the simulation. A spread in the breakdown voltage is

observed in the measurement. Due to the spatial limitation of lithography, the tip of the 2HMs varies across the wafer. On some sensors, the tips are rounder than the others, thus have a lower peak electric field. This effect does not matter for the F3D configuration as the shape of the P+ ring does not change due to variation of lithography.

As discussed in Section IV-A, one key challenge in the F3D design is the integrity of the metal bus lines. This effect can, in fact, be observed in the  $I - V$  measurements as shown in Fig. 16. For devices with broken metal bus lines, the magnitude of the leakage current does not equal to the total leakage current in all 2500 SVs ( $50 \times 50$ ) since not all SVs were connected. A lower leakage current is, therefore, observed. In Fig. 16, the  $I - V$  of six devices have similar characteristics, while three devices behave very differently. The six devices reach a current saturation at low voltage and

hit breakdown at around 20 V. The other three “outliners” have extremely low current and are most likely to be devices that have broken metal bus lines. The gradual and higher breakdown was also an indication. Broken metal lines are poor connections. If the first SV connecting to the measurement pad has broken or semibroken lines, one measures close to zero current. When one reaches a high enough voltage, a current can spark across the poor connection. This then generates a gradual current increase and eventually when the connection is “good” enough, breakdown occurs but is independent of the actual breakdown of the sensors. Although there seems to be a clear distinction in the  $I - V$  measurements between the devices with and without broken metal bus lines, one can still not be certain that the other six devices have no disconnected SVs. In fact, the variations in the leakage current amongst the six “good” devices might also be caused by disconnected SVs. Electrical measurements are, therefore, not a reliable method, and the fabrication yield must be determined entirely by visual inspection. In our first prototype run, optical inspection was used to select good devices for further functional characterization.

In the first prototype run, two wafers were processed for the realization of full 3-D F3DM. The measured  $I - V$  on the two devices are shown in Fig. 17. The  $I - V$  measurements are not so dissimilar to the F3D devices (Fig. 16) before this extra process. This demonstrated the experimental process of removing excess silicon outside the SVs, and planarizing with a layer of polyimide was successful. These devices were diced, mounted, and assembled for functional testing.

The results from the first prototype run provided useful information for technology optimization. Using these results, a larger diameter of 25  $\mu\text{m}$  and less thermal treatment were implemented in the second and the third prototype runs. A longer effective interelectrode distance implies a higher breakdown voltage which was also shown by the simulation results for larger SVs. The measured  $I - V$  from several F3D devices obtained from the third prototype run with larger SVs are shown in Fig. 18. The measurements are in excellent agreement with the simulated results. The measured devices, each has 4000 SVs ( $20 \times 20$ ), can be compared directly and in a good agreement with the simulated  $I - V$  shown in Fig. 4. Both the simulated and measured currents are in the order of 10–20 pA above the full depletion voltage. Similarly, both the simulated and measured breakdown voltages are about 30 V. In both the second and third prototype runs, different process parameters were adjusted and optimized to reduce broken metal lines, and this was clearly improved, and many more devices have intact metal lines. However, disconnection remains a key yield factor. In the coming prototype runs, further design and process optimizations will be carried out to further address this issue.

### C. Radiation Measurements

Devices were selected for functional characterization based on electrical measurements and optical inspections. Charge collection dynamics inside the SVs was a key study to understand the functionality of the SV and to verify the minimum

crosstalk and the well-defined sensitivity, promised by the unique design of F3D and F3DM. Tests were conducted at various facilities with different radiation types. The experiment reported here was performed at the ID21 beamline at the European Synchrotron Facility (ESRF). The devices under test is of F3DM configuration, where the circular trenches were closed and filled with polysilicon, and the excess silicon around the SVs was removed and replaced with polyimide (F3DM). The experiment was carried out using the scanning X-ray microscope (SXM) available at ID21. A beam energy of 7.2 keV was focused to a spot size of about  $0.4 \times 1.0 \mu\text{m}^2$  on the sensor surface.

The sensor was mounted on a custom-designed printed circuit board (PCB), and wire-bonded for biasing and signal readout. The PCB was then mounted on the positioning stage of the SXM and was scanned across the beam in steps of 0.5  $\mu\text{m}$ . The beam intensity was moderated using attenuators to avoid the generation of excess charge into the sensor. The sensor was reverse-biased during the scan and its output current was monitored using an electrometer. The measured signal intensity was corrected for beam variations using monitoring sensors upstream and downstream from the sensor under test in the beamline.

The SXM at beamline ID21 is equipped with a fluorescence detector that provides accurate information on the material found under the beam at any given position. This was a very important feature during the experiment as it allowed the correct identification of the desired scanning location. In Fig. 19(a), it is possible to distinguish clearly the sensors’ metal lines as shown in a beige color, where the silicon and poly-Si is shown as gray and the lack of excess material outside the SV is shown as black. The induced current signal read by the device during the scan is shown in Fig. 19(b) where the device was biased at a voltage of 50 V. A raster scan requires a long data taking time to produce good images. The data obtained using 50 V is shown in this article in which the data was taken overnight. Unfortunately, there was no sufficient beam times to repeat the same for lower voltages.

The results show that the active volume of the sensitive element is extremely well defined and uniform, with a small decrease in efficiency observed only at the center of the SV. At the central N<sup>+</sup> electrode, charge carriers were lost to recombination due to the high concentration of N-type dopants in the electrode. The obtained result shows that the diameter of the SV is about 26  $\mu\text{m}$  full-width at half-maximum (FWHM), as reported in Fig. 19. For this device under test, the diameter was designed to be 30  $\mu\text{m}$  on the photolithographic mask layers. The measured result is as expected as the radius was predicted to be around 25–26  $\mu\text{m}$  after dopant diffusion. In the horizontal direction, a slight smearing of readout signal was observed that is caused by the tilted sensor stage at ID21, as it is oriented at a 30° angle with respect to the beam. The parameter was fixed during the experiment.

The time response and signal collection were also studied using fast transimpedance amplifiers and an oscilloscope. The signal acquisition was triggered by the beam line at

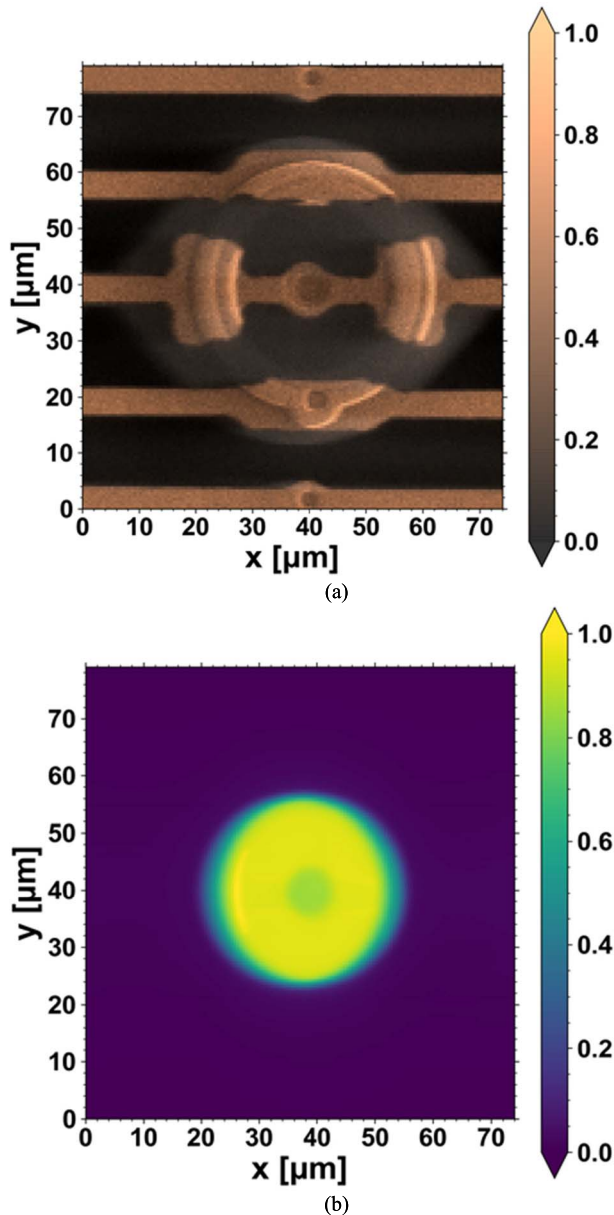


Fig. 19. Measurement results from X-ray beam scanning at a bias voltage of 50 V. The fluorescence signal in (a) shows the location of the beam on the sensor, while the sensor signal (b) shows the signal efficiency across one SV.

the arrival of each electron bunch and the oscilloscope automatically acquired time evolution of the current pulse coming from the sensor. It was observed that full charge collection is achieved in less than 15 ns even when the device was at zero bias voltage. The minimum charge collection time was measured to be  $\sim 5$  ns with a bias voltage of 50 V. Members of our team have also done extensive functional measurements with respect to charge collection, RBE, and particle therapy, and the results can be found in [20] and [22]–[27].

This experiment together with the electrical characterization clearly demonstrates the fabricated sensors operate as expected, confirming the expected results from numerical simulation throughout the prototyping phase.

## V. CONCLUSION

Fabrication of full 3-D microdosimeters is a unique technology that combines the radiation detector and MEMS techniques. Three-dimensional microdosimeters with various designs, including half-moons (2HM), full 3-D with fully encapsulated SVs (F3D), and full 3-D mushroom (F3DM) were successfully fabricated and characterized. Three-dimensional microdosimeters were demonstrated to have low depletion voltage. The first electrical and functional testing verifies the performance characteristics of F3D microdosimeters, well-defined SVs, and near-zero crosstalk. Hence, the technology plan was fully verified. Measurements using a fine X-ray radiation beam demonstrated the uniform charge collection within the well-defined SV. The completed devices function as expected and their measured characteristics are in excellent agreement with the simulation results, confirming the success of optimal design approach and a new fabrication technology. The results confirmed that 3-D microdosimeters offer promising performance characteristics for charge particle detection. The F3DM devices, which is the ultimate design with fully encapsulated SVs embedded in a tissue equivalent material was a successful implementation. However, optical and electrical measurements indicated that the overall yield must further be improved to bring the technology onto manufacturing level. The major yield factor is to maintain a high integrity of metal bus lines that read out the central N+ electrodes. Future optimization must be carried out to bring this technology into maturity. Future prototype runs will focus on optimizations, reliability, and fine tuning the final polyimide deposition process. The optimization will aim to deliver a technology plan that offers a high yield throughput for both F3D and F3DM microdosimeters.

## ACKNOWLEDGMENT

The authors would like to thank fabrication engineers Leny Nazareno and Ane Carine Lund for their valuable assistance throughout the fabrication of these prototypes. The authors also thank the European Synchrotron Radiation Facility for the provision of beamline facilities and the staff, in particular, Murielle Salome, for their assistance in using the ID21 beamline.

## REFERENCES

- [1] H. H. Rossi and M. Zaider, *Microdosimetry and Its Applications*. London, U.K.: Springer, 1996.
- [2] D. Srdoc, "Experimental technique of measurement of microscopic energy distribution in irradiated matter using Rossi counters," *Radiat. Res.*, vol. 43, no. 2, pp. 302–319, 1970.
- [3] V. Conte, P. Colautti, S. Chirriotti, D. Moros, M. Ciocca, and A. Mairani, "Mini-TEPC microdosimetric study of carbon ion therapeutic beams at CNAO," in *Proc. EPJ Web Conf.*, vol. 153, 2017, p. 01012.
- [4] P. D. Bradley, A. B. Rosenfeld, and M. Zaider, "Solid state microdosimetry," *Nucl. Instrum. Meth. Phys. Res. B, Beam Interact. Mater. At.*, vol. 184, nos. 1–2, pp. 135–157, 2001.
- [5] P. D. Bradley, A. B. Rosenfeld, K. K. Lee, D. N. Jamieson, G. Heiser, and S. Satoh, "Charge collection and radiation hardness of a SOI microdosimeter for medical and space applications," *IEEE Trans. Nucl. Sci.*, vol. 45, no. 6, pp. 2700–2710, Dec. 1998.
- [6] P. D. Bradley, "The development of a novel silicon microdosimeter for high LET radiation therapy," Dept. Eng., Univ. Wollongong, Keiraville, NSW, Australia, Tech. Rep. 1367, 2000.

- [7] A. L. Ziebell *et al.*, "A cylindrical silicon-on-insulator microdosimeter: Charge collection characteristics," *IEEE Trans. Nucl. Sci.*, vol. 55, no. 6, pp. 3414–3420, Dec. 2008.
- [8] W. H. Lim *et al.*, "Cylindrical silicon-on-insulator microdosimeter: Design, fabrication and TCAD modeling," *IEEE Trans. Nucl. Sci.*, vol. 56, no. 2, pp. 424–428, Apr. 2009.
- [9] N. S. Lai, W. H. Lim, A. L. Ziebell, M. I. Reinhard, A. B. Rosenfeld, and A. S. Dzurak, "Development and fabrication of cylindrical silicon-on-insulator microdosimeter arrays," *IEEE Trans. Nucl. Sci.*, vol. 56, no. 3, pp. 1637–1641, Jun. 2009.
- [10] J. Livingstone *et al.*, "Large area silicon microdosimeter for dosimetry in high LET space radiation fields: Charge collection study," *IEEE Trans. Nucl. Sci.*, vol. 59, no. 6, pp. 3126–3132, Dec. 2012.
- [11] A. Rosenfeld, "Method and apparatus for tissue equivalent solid state microdosimetry," U.S. Patent EP 21026854 A, Dec. 19, 2007.
- [12] S. I. Parker, C. J. Kenney, and J. Segal, "3D—A proposed new architecture for solid-state radiation detectors," *Nucl. Instrum. Meth. Phys. Res. A, Accel. Spectrom. Detect. Assoc. Equip.*, vol. 395, no. 3, pp. 328–343, Aug. 1997.
- [13] T.-E. Hansen *et al.*, "First fabrication of full 3D-detectors at SINTEF," *J. Instrum.*, vol. 4, no. 3, Mar. 2009, Art. no. P03010.
- [14] A. Kok *et al.*, "Fabrication of 3D silicon sensors," in *Proc. Vertex Conf. Sci. (PoS)*, Loch Lomond, U.K., Jun. 2010.
- [15] G.-F. D. Betta *et al.*, "Development of 3D-DDTC pixel detectors for the ATLAS upgrade," *Nucl. Instrum. Meth. Phys. Res. Sect. A, Accel., Spectrometers, Detectors Associated Equip.*, vol. 636, pp. S15–S23, Apr. 2011.
- [16] G. Pellegrini *et al.*, "3D double-sided detector fabrication at IMB-CNM," *Nucl. Instrum. Meth. Phys. Res. Sect. A, Accel., Spectrometers, Detectors Associated Equip.*, vol. 699, pp. 27–30, Jan. 2013.
- [17] J. X. J. Zhang and K. Hoshino, *Molecular Sensors and Nanodevices*. Norwich, NY, USA: William Andrew Applied Science Publishers, 2014, pp. 43–101.
- [18] C. Fleta *et al.*, "3D cylindrical silicon microdosimeters: Fabrication, simulation and charge collection study," *J. Instrum.*, vol. 10, no. 10, Oct. 2015, Art. no. P10001.
- [19] M. J. Cameron *et al.*, "Characterization of 3-D-mesa silicon single strip detectors for use in synchrotron microbeam radiation therapy," *IEEE Trans. Radiat. Plasma Med. Sci.*, vol. 4, no. 4, pp. 470–478, Jul. 2020.
- [20] L. T. Tran *et al.*, "The relative biological effectiveness for carbon, nitrogen, and oxygen ion beams using passive and scanning techniques evaluated with fully 3D silicon microdosimeters," *Med. Phys.*, vol. 45, no. 5, pp. 2299–2308, May 2018.
- [21] *Synopsys TCAD Tools*. Accessed: 2020. [Online]. Available: <https://www.synopsys.com/silicon/tcad.html>
- [22] B. James *et al.*, "SOI thin microdosimeters for high LET single-event upset studies in Fe, O, Xe, and cocktail ion beam fields," *IEEE Trans. Nucl. Sci.*, vol. 67, no. 1, pp. 146–153, Jan. 2020.
- [23] L. T. Tran *et al.*, "Thin silicon microdosimeter utilizing 3-D MEMS fabrication technology: Charge collection study and its application in mixed radiation fields," *IEEE Trans. Nucl. Sci.*, vol. 65, no. 1, pp. 467–472, Jan. 2018.
- [24] B. James *et al.*, "3D sensitive volume microdosimeter with improved tissue equivalency: Charge collection study and its application in 12C ion therapy," *J. Phys., Conf. Ser.*, vol. 1154, Jan. 2019, Art. no. 012012.
- [25] Z. Pastuovic *et al.*, "IBIC microscopy—the powerful tool for testing micron-sized sensitive volumes in segmented radiation detectors used in synchrotron microbeam radiation and hadron therapies," *Nucl. Instrum. Meth. Phys. Res. Sect. B, Beam Interact. Mater. At.*, vol. 458, pp. 90–96, Nov. 2019.
- [26] L. T. Tran *et al.*, "In-field and out-of-file application in 12C ion therapy using fully 3D silicon microdosimeters," *Radiat. Meas.*, vol. 115, pp. 55–59, Aug. 2018.
- [27] B. James *et al.*, "SOI thin microdosimeter detectors for low-energy ions and radiation damage studies," *IEEE Trans. Nucl. Sci.*, vol. 66, no. 1, pp. 320–326, Jan. 2019.